


RESEARCH ARTICLE | JUNE 02 2023

## Evolution of colloidal coatings due to a wetting and drying process **FREE**

Special Collection: [Paint and Coating Physics](#)

Ludovic Pauchard 

 Check for updates

*Physics of Fluids* 35, 067107 (2023)

<https://doi.org/10.1063/5.0153415>



View  
Online



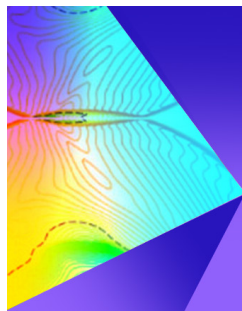
Export  
Citation

[CrossMark](#)

### Articles You May Be Interested In

The effect of size ratio on the sphere structure factor in colloidal sphere-plate mixtures

*J. Chem. Phys.* (November 2012)



## Physics of Fluids

### Special Topic: Shock Waves

**Submit Today!**

# Evolution of colloidal coatings due to a wetting and drying process

Cite as: Phys. Fluids **35**, 067107 (2023); doi: [10.1063/5.0153415](https://doi.org/10.1063/5.0153415)

Submitted: 7 April 2023 · Accepted: 16 May 2023 ·

Published Online: 2 June 2023



View Online



Export Citation



CrossMark

Ludovic Pauchard<sup>a)</sup> 

## AFFILIATIONS

Université Paris-Saclay, CNRS, FAST, 91405 Orsay, France

Note: This paper is part of the special topic, Paint and Coating Physics.

<sup>a)</sup> Author to whom correspondence should be addressed: [ludovic.pauchard@u-psud.fr](mailto:ludovic.pauchard@u-psud.fr)

## ABSTRACT

Paints and coatings are usually made by depositing a volatile liquid containing dispersed colloidal particles. The dry film is obtained through the evaporation of the volatile liquid. Depending on the ability of the particles to deform under capillary effect, we show that the drying can yield continuous coatings with no porosity, uniform porous coatings, or the formation of singularities, such as cracks causing the final film to be non-uniform. The evolution of the resulting coatings is then subjected to a wetting and drying process. Wetting leads to an increase in the water content of the unsaturated porous coating while drying results in water reduction. The response of the coatings to such a process can exhibit slight or significant changes in the morphology of the coatings that are related to their rheological properties. In particular, the growth of blisters is reported during the wetting and drying process.

Published under an exclusive license by AIP Publishing. <https://doi.org/10.1063/5.0153415>

## I. INTRODUCTION

Drying processes are often used to create coatings on the surfaces of solid materials. Typically, a liquid dispersion of fine particles in a volatile liquid is applied to the surface of the solid. Then, the liquid phase is evaporated to yield a dense solid film. The rheology of colloidal dispersions varies from viscous to elasto-visco-plastic to brittle when their water content decreases.<sup>1</sup> The properties of the particles that compose the coating also determine its macroscopic behavior.<sup>2–4</sup> Therefore, under the capillary effect, the drying can yield continuous coatings with no porosity, uniform porous coatings, or the formation of singularities, such as cracks, causing the final film to be non-uniform. The resulting patterns can evolve when the coatings are subjected to further solicitations. We study in this work the response of the coatings when subjected to a wetting and drying process. Wetting is defined as the process leading to an increase in the water content of an unsaturated porous coating while drying is defined as the process leading to a reduction in water.

In general, the behavior of coatings through drying has been a source of tough conceptual problems and also irritating practical difficulties for more than a century. Hence, the success of the coating procedure is crucial to the properties of the coated material because it provides it with new functionalities. Common examples are paints, cosmetics, optical coatings on glass, and anti-corrosion coatings on metals. Depending on the applications, the coatings undergo various

stresses, starting with the drying stress at the origin of the film formation. Hence, coatings may undergo various kinds of instabilities, which may induce surface wrinkling, creasing, folding, blistering, or cracking.<sup>5</sup> Some patterns are shown in Fig. 1. These phenomena are traditionally considered to be flaws in performance, including reductions in mechanical properties and esthetics, for which there have been much effort and more trials to avoid. Moreover, the resulting patterns can evolve due to a variety of mechanisms, including mechanical loading, thermal expansion and contraction, and humidity changes, especially in particulate coatings.

In this way, the present work is based on coatings of colloids with different capacities to deform. In the case of latex particles, chemical properties provide different glass-transition temperatures. The resulting coatings exhibit various mechanical properties during drying at room temperature. The medium can vary from elasto-visco-plastic to brittle. In particular, different mechanisms are involved.<sup>7,8</sup> In contrast to latex particles, silica is much stiffer. The resulting coatings are possibly brittle. In any case, the particle size is similar from one system to the other except in the case of silica particles (Ludox HS), which are considered here because they are known to possess high mechanical strength and stiffness, making them suitable for use in films with higher mechanical response.<sup>9–11</sup> Depending on the properties of the films as well as the presence of cracks in the dry coatings, we focus here on the effect of the wetting and drying process on the evolution

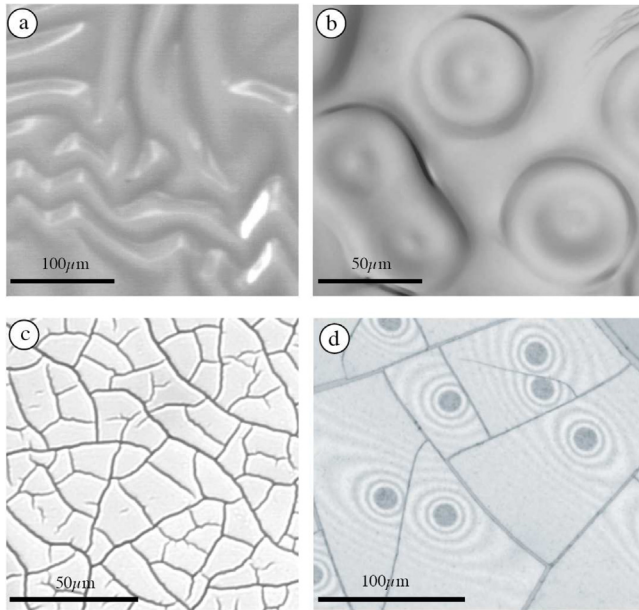


**FIG. 1.** Images of various morphologies resulting from the drying of aqueous dispersions of colloids: (a) pattern of folds, (b) buckled blisters, (c) channeling cracks, and (d) transparent film partially delaminated from the substrate as indicated by the interference fringes.<sup>6</sup>

of singularities. The response of the coatings to such a process can exhibit slight or significant changes in the morphology of the coatings that are related to their rheological properties. In particular, in the case of porous films composed of soft particles, the wetting and drying process leads to the formation of blisters when the colloidal film delamination from the substrate. These last grow and reach a well-defined size, which is analyzed experimentally and by considering the energies involved.

**II. EXPERIMENTAL**

**A. Colloidal dispersions**

In the present work, aqueous dispersions of organic and inorganic particles are considered. The former consists of waterborne latex

particles provided by Rhodia Recherche, Aubervilliers, France. In the absence of evaporation, the dispersions are stable due to their characteristic Brownian motion. After spreading and drying under ambient temperature and humidity conditions, the mechanical properties of the films are strongly affected by the glass transition temperature,  $T_g$ , of the particles. Hence, different latex dispersions are considered. Their main characteristics are reported in Table I. In particular, at room temperature, hard particles with  $T_g = 100$  °C are made of a styrene copolymer and acrylic acid while soft particles with  $T_g = 0$  °C are made of a copolymer of styrene and carboxylated butadiene. The latex particles were synthesized in the presence of sodium dodecyl sulfate (SDS).

The inorganic particles are silica particles (Ludox HS-40 and klebosol purchased from Sigma-Aldrich). The main characteristics are reported in Table I. For each system, the particles are polydisperse enough not to crystallize.

**B. Coatings formation**

The substrates are microscope glass slides carefully cleaned with pure water and then with ethanol before being dried in a heat chamber at 100 °C. The substrate preparation allows fairly good wetting reproducibility. The wetting of a colloidal drop deposited on the substrate allows us to estimate the thermodynamic work of adhesion of the colloidal film on the substrate. Hence, the work of adhesion,  $\Gamma_{adh}$ , can be deduced from the Dupré formula, which relates the surface tension of a liquid drop  $\gamma_l$  and the static contact angle  $\theta_0$ :  $\Gamma_{adh} = \gamma_l(1 + \cos \theta_0)$ .<sup>12</sup> The values of  $\Gamma_{adh}$  are reported in Table I.

A volume of the colloidal solution is deposited at the surface of the substrate and is then spread across by a steel bar coater. This last exhibits a gap clearance,  $h_g$ , that subsequently determines the thickness of the deposited film. In this way, three gap clearances are used:  $h_g = 10, 20,$  and  $40 \mu\text{m}$ . This film applicator leaves a liquid film of thickness  $h_i$  when the bar is moved gently and manually in a single direction until the substrate is evenly covered [Fig. 2(a)]. At this stage, the thickness of the liquid film is not precisely measured but the dry coating is. Since the film surface is exposed to air evaporation of the water starts as soon as the film is applied. Evaporation is carried out at room temperature and humidity rate  $RH = 50\% \pm 5\%$ . Under these conditions, the transfer of water in the air is limited by diffusion in the surrounding air (absence of convection in the vapor). Observation is performed using a DM2500 Leica microscope with objective 5 $\times$  and

**TABLE I.** Main characteristics of the colloidal dispersions considered in the present work: glass transition temperature,  $T_g$ , particle size (estimated using diffusion light scattering), polydispersity index, solid content (\* measurements after dilution with pure water Milli-rho), the surface tension of the liquid phase  $\gamma_l$  (estimated using Wilhelmy techniques), static contact angle  $\theta_0$  (from side viewed images of sessile drops), and adhesion energy estimated using the Dupré equation.

Colloids	Particle size (nm)	$T_g$ (°C)	Polydispersity index	Particle volume fraction (%) (* $\pm 2\%$ )	$\gamma_l$ (mN/m)	$\theta_0$ (°)	$\Gamma_{adh}$ (N/m)
Latex	97	0	0.07	30*	57 $\pm$ 4	82 $\pm$ 4	0.06
Latex	88	16	0.06	30*	52 $\pm$ 3	78 $\pm$ 4	0.06
Latex	85	25	0.06	30*	55 $\pm$ 5	75 $\pm$ 4	0.07
Latex	93	40	0.08	30*	51 $\pm$ 4	79 $\pm$ 4	0.06
Latex	85	100	0.07	30*	53 $\pm$ 4	76 $\pm$ 4	0.07
Klebosol	79	...	0.14	28	67 $\pm$ 5	28 $\pm$ 4	0.13
Ludox HS40	14	...	0.16	24	64 $\pm$ 5	32 $\pm$ 4	0.12

Downloaded from http://pubs.aip.org/aip/pof/article-pdf/doi/10.1063/5.0153415/17937586/067107\_1\_5.0153415.pdf

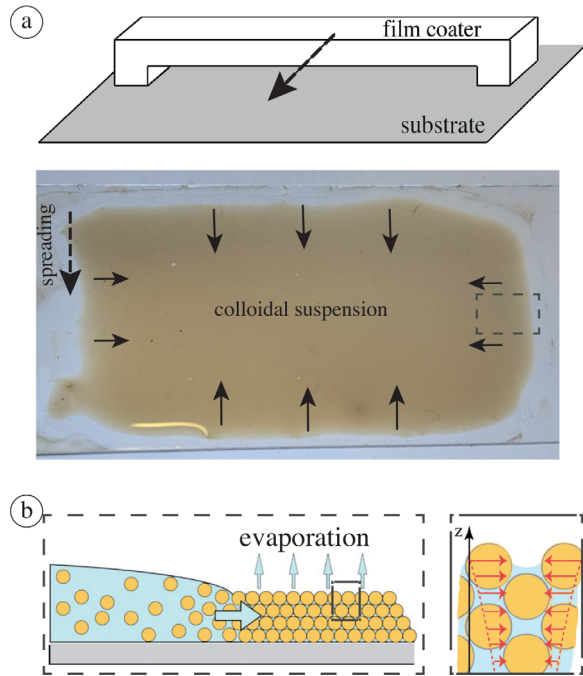


**FIG. 2.** (a) Sketch and image in top view of the colloidal film deposition (lateral size of the deposit: 25 mm). (b) The evaporation from the surface of the dispersion drives a solidification front. Right: the red arrows depict the pressure gradient in the structure as a result of the capillary effect.

50× magnifications for global view and close-up view (envelope thickness measurements), respectively. The thickness of the dry coating is estimated by differential focus at the film/substrate and film/air interfaces using an optical microscope allowing for the accuracy of ± 2 μm.

**C. Drying kinetics**

A volume of 70 μl of dispersion is deposited in a circular container (diameter ~10 mm and height ~1 mm). The bottom of the container is a carefully cleaned glass substrate, while the lateral wall is a silicone seal [Fig. 3(a)]. The contact line of the solution remains quenched at the upper edge of the container during the drying process. As a result, a film of approximately constant thickness is formed in the center of the container (70% of the total surface area). The mass variation with time is measured with a precision scale (Sartorius). The

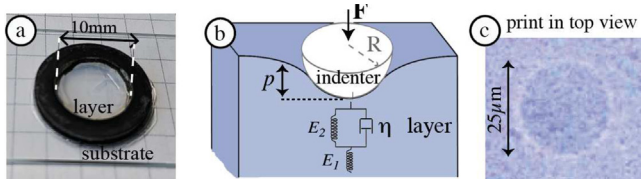


**FIG. 3.** (a) Geometry used to characterize the drying kinetics and mechanical properties of the colloidal layer. (b) Sketch of the indentation test using a spherical indenter tip for creep measurements. (c) Print left at the surface of the solid layer by the indentation test after removing the indenter tip.

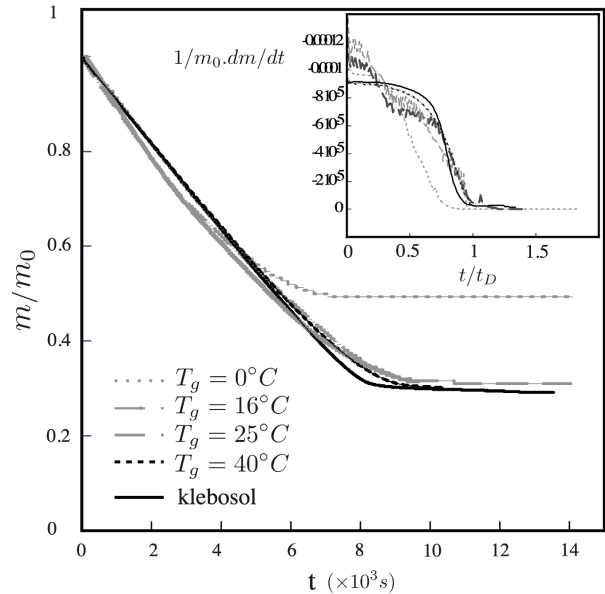


**FIG. 4.** Drying curves for different films of latex particles and klebosol particles: mass variation with time. Inset: time variation of the drying rate.

drying rate is then extracted from the mass measurements (Fig. 4). The drying of colloidal dispersion is usually separated into three periods, to which physical processes have been usually associated.<sup>13</sup> In the first stage, the water evaporates at a constant rate close to that of an electrolyte water solution. In general, the constant rate drying period is followed by a nonlinear drying rate period where the drying rate decreases. The third period is usually said to enter the second “falling rate period,” which completes the drying process.

**D. Mechanical characterization of the coatings**

The viscoelastic properties of the dry coatings are quantified using indentation testing (micro-indenter from Anton Paar). Measurements are performed on planar dry layers, 200 μm thick, using the same geometry reported in Fig. 3(a). Indentation testing consists of the penetration of a spherical tip radius assumed perfectly rigid inside the sample by applying a controlled force. In particular, we proceed in this work to creep measurements. Creep experiments involve the application of a constant applied force,  $F_0$ , and the subsequent measurement of penetration depth,  $p$ , as a function of time [see sketch in Fig. 3(b)]. A spherical tip of radius  $R = 0.25$  mm is first driven inside the sample with a fixed loading speed of 50 mN/min. When the applied force  $F_0 = 50$  mN is reached, the penetration depth  $p$  is measured as a function of time at constant loading,  $F_0$  (Fig. 5). After removing the indenter tip, a typical view of the print on the coating can be observed in Fig. 3(c). For each layer, the measurements are carried out after a delay time defined by the study of the drying kinetics. Indeed, creep investigation starts at the beginning of the second “falling rate period;” this avoids the formation of cracks due to the contact of an indenter tip during the measurements.

Another material property of interest is the yield stress,  $\sigma_Y$ , that determines the ability of the coating to resist or not to solicitations.

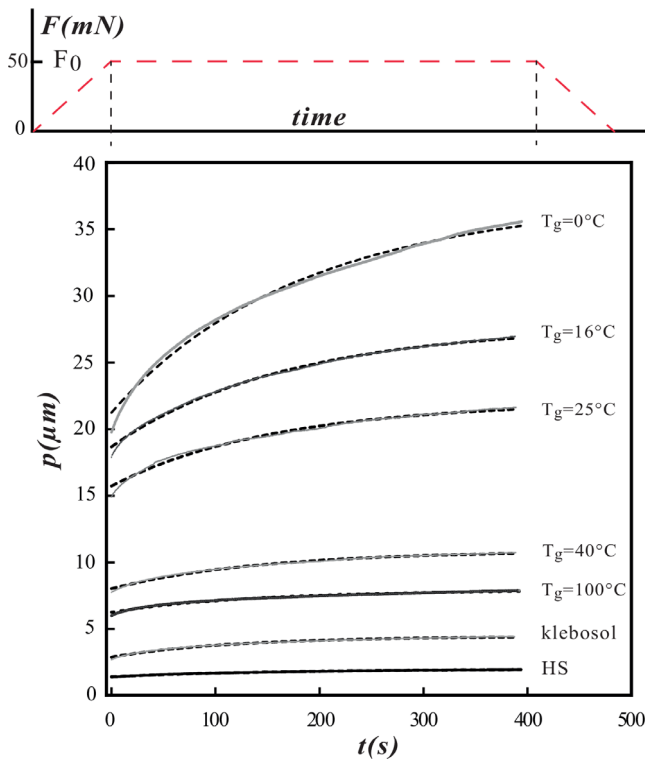


**FIG. 5.** Indentation creep behavior of the colloidal layers of investigation. Above: protocol for measurement of viscoelastic behavior with an applied force,  $F_0$ , held constant. Main graph: time variation of the penetration depth,  $p$ , for different coatings. The rheological behavior of the layer is characterized by a “Zener” model where a spring is connected in series with a combination of spring and damper [see Fig. 3(b)].

The compressive yield stress is estimated in the dry coatings using indentation testing (see the method in Appendix A). Results for the coatings are reported in Tables II and III.

**E. Wetting and drying process**

The evolution of dry coatings under the effect of the wetting and drying process is investigated. This process occurs at room temperature and humidity rate  $RH = 50\% \pm 5\%$ . The wetting process consists in depositing a water drop of  $3 \mu\text{l}$  at the surface of a dry coating using

**TABLE II.** Main viscoelastic properties of the latex films obtained from measurements in Fig. 5 and the fit Eq. (2). The accuracy of the moduli obtained using Eq. (2) is of the order of 5%. The accuracy of the yield stress is of the order of 5% (see Appendix A).

$T_g$ ( $^{\circ}\text{C}$ )	$E_1$ (MPa)	$E_2$ (MPa)	$\tau$ (s)	$\sigma_Y$ (MPa)
0	27	22.2	209	1.1
16	32	40	182	4.8
25	42	64	170	5.4
40	86	98	150	6.3
100	169	400	140	36.0

**TABLE III.** Main viscoelastic properties for silica films obtained from measurements in Fig. 5 and the fit with Eq. (2). The accuracy of the moduli obtained using Eq. (2) is of the order of 5%; the accuracy of the yield stress is of the order of 5% (see Appendix A).

	$E_1$ (GPa)	$E_2$ (GPa)	$\tau$ (s)	$\sigma_Y$ (MPa)
Klebosol	0.5	0.6	125	24.0
HS	1.6	2.3	82	40.4

a micropipette. In the case of a porous surface, the imbibition process in the coating takes place even if a part of the drop is still on the coating surface and evaporates into the surrounding air. The drying process naturally starts during the imbibition process and continues after the liquid is entirely imbibed into the layer. Observation uses reflected light microscopy to observe the singularities, such as cracks or blisters, that can develop on the surface of the coating.

**III. RESULTS AND DISCUSSION**

**A. Dry coatings of colloids exhibiting various poroviscoelastic properties**

When a colloidal dispersion is applied to the substrate, the water starts to evaporate. Hence, the drying timescale of the film is defined as

$$t_D = \frac{h_i}{V_E}, \tag{1}$$

where  $h_i$  is the initial film thickness and  $V_E$  is the evaporation rate. The film exhibits an edge around its entire perimeter as a result of a strong anchoring of the three-phase line on the glass slide. A drying front is generated from this edge and progresses directionally toward the middle of the film as described in Fig. 2(a). This drying front results from the accumulation of particles. This front is associated with the formation of a transition region.<sup>14</sup> A wet film of close-packed particles is then formed at a particle volume fraction  $\phi_m \sim 0.6$ . As water evaporates, the surface menisci form: a pressure gradient builds up induced by the capillary effect [see the sketch in Fig. 2(b)]. This effect governs the coating shrinkage. At this point, the evolution of the coatings upon drying can take different routes depending on the physical properties of the films. These properties are determined by those of the particles involved. In particular, some of the properties of viscoelastic materials are their ability to creep, recover, undergo stress relaxation, and absorb energy. In this way, the creep behavior is reported for the different coatings under consideration in Fig. 5. A linear viscoelastic model, e.g., Zener model, is used to quantify the creep experimental results [see the sketch in Fig. 3(b)]. This model accounts for an instantaneous elastic deformation when stress is applied and a creep deformation that tends to a limit at constant stress. The creep strain is expressed as

$$p^{3/2}(t) = \frac{3}{4\sqrt{R}} F_0 (E_1^{-1} + E_2^{-1} (1 - \exp[-t/\tau])), \tag{2}$$

where  $E_1$  can be interpreted as short-time elasticity (purely elastic spring) and  $E_2$  as long-time elasticity (purely elastic spring connected in parallel to a purely viscous damper). The  $E_1$  elasticity is adjusted to account for the indentation formed at a short time by the rapid increase in load. The  $E_2$  elasticity and viscosity are used to describe the

flow of our material (particle deformation) over a long time period when a constant force,  $F_0$ , is applied.<sup>15</sup> The flow of the material over a long time period is involved in the relaxation time  $\tau$ . Note that this model is particularly relevant for glassy polymers.

As a result, the main viscoelastic properties deduced from creep measurements are reported in Tables II and III. The accuracy of the moduli and the relaxation time obtained using Eq. (2) are of the order of 5%.

The viscoelastic properties of the films determine the extent of deformation during the film formation. Hence, at the final stage of the drying, the films can be free of cracks or exhibit crack patterns (images (a)–(e) in Fig. 6. For thin coatings, the cracks form isolated short lines

(image (b) in Fig. 6). For thicker coatings, the cracks form a regular network of singularities invading the layer during the drying process as shown in the images (c)–(e) in Fig. 6. These patterns are related to the mechanical response of the film to stresses that develop during the drying. The coatings' morphologies are mapped in the diagram in Fig. 6 as a function of the drying timescale,  $t_D$ , which is governed by the film thickness (at a constant evaporation rate  $5 \times 10^{-8}$  m/s) and the relaxation timescale,  $\tau$ , characteristic of the viscoelastic behavior of the coatings. Except in the case of isolated crack forms, no significant change is revealed by changing the thickness of the layer, e.g., the drying timescale, in the range of thicknesses considered in this work.

As mentioned above, the final aspect of the coating made of soft latex particles is homogeneous (image a in Fig. 6). This behavior is indicated by the hatched area of the diagram (Fig. 6): films of particles with a glass transition temperature of 0, 16, and 25 °C in the range of thicknesses considered here. Under the influence of the capillary effect, the deformation of soft particles is facilitated during the film formation at room temperature.<sup>17</sup> The deformation regime was clearly investigated as a function of several key parameters in the pioneering work of Routh and Russel.<sup>7,8</sup>

Indeed, the deformation of soft particles can result in closing all the voids more or less partially at the exposed surface without inducing a crack. This process is significant in the case of coatings of particles with  $T_g = 0$  °C and is highlighted by the drying kinetics in Fig. 4. The decrease in the mass variation with time is slowed down earlier than for the other coatings ( $T_g = 16, 25, 40, 100$  °C). Moreover, at the end of the drying, the final mass of the film containing soft particles ( $T_g = 0$  °C) is larger than in the case of other systems. These results suggest that a significant amount of water remains trapped in the film while the surface exposed to air becomes impermeable to water.

In the case of stiffer particles, the response of the close-packed particles to capillary effects can lead to different situations allowing the recovery of elastic energy. For thin films, a few micrometers thick, no cracks are usually observed: the elastic energy stored in the film is too weak to overcome the fracture energy.<sup>7,18,19</sup> This is observed in the dry films of particles with  $T_g = 40$  °C. For thicker films, the films usually crack to release stress. Isolated cracks nucleate in the film, over a length that scales with the film thickness (h) (image b in Fig. 6). For still thicker films, as the films dry, a pattern of cracks forms in the “wet” region of the films and propagates in a direction perpendicular to the drying front. The cracks exhibit a well-defined spacing that depended upon several parameters in particular, the local colloid film thickness.<sup>20–22</sup> Such a pattern of cracks is also observed in the case of films made of particles with  $T_g = 100$  °C (image c in Fig. 6) as well as silica particle (images d and e in Fig. 6). In general, the crack spacing in coatings scales with the thickness. Different theoretical models have been established, in particular in the case of a network of parallel cracks<sup>22</sup> and in the case of an isotropic crack pattern.<sup>23</sup> The crack spacing,  $\lambda$ , can be derived using the Griffith criterion by equating the strain energy stored in a volume confined between two parallel cracks of length  $l$ , says  $\lambda hl$ , with the energy required to create new crack surfaces

$$1/2E\epsilon^2 \lambda al = 2\Gamma hl, \tag{3}$$

where  $\Gamma$  is the surface energy of the particle material assumed to be equal to the surface tension of the liquid phase in the gel. In Eq. (3), we assume that the stresses are generated in a layer of thickness,  $a$ , within the coating and that the cracks extend throughout the

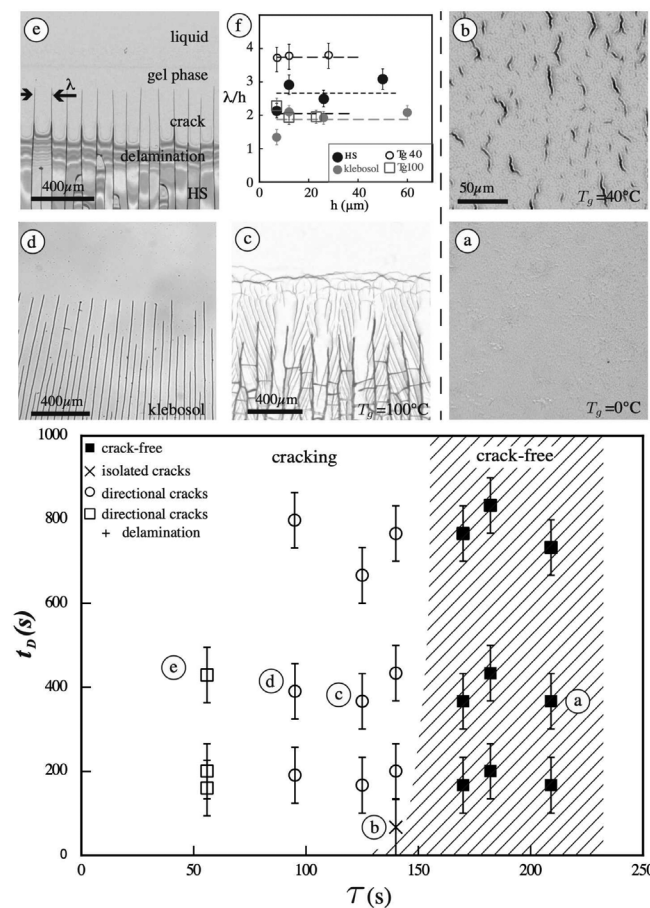


**FIG. 6.** Typical patterns form during the drying. (a) Crack-free surface (film of particles  $T_g = 0$  °C), (b) isolated cracks (film of particles  $T_g = 40$  °C), (c)–(e) network of parallel cracks propagating directionally upwards (with creases<sup>16</sup> for latex films— $T_g = 100$  °C or delamination process for silica films—silica HS40). (f) Dimensionless crack spacing,  $\lambda/h$ , as a function of the coating thickness,  $h$  (the values of the crack spacing are averaged over ten measurements for each coating thickness). Data are shown for the coatings exhibiting a network of parallel cracks during the drying. Graph: diagram mapping the final aspects of the films displayed following the drying timescale,  $t_D$ , and the relaxation timescale,  $\tau$ . The hatched area corresponds to the crack-free films at the microscope's optical resolution while the symbols  $\times$ ,  $\circ$ ,  $\square$  indicate crack patterns.

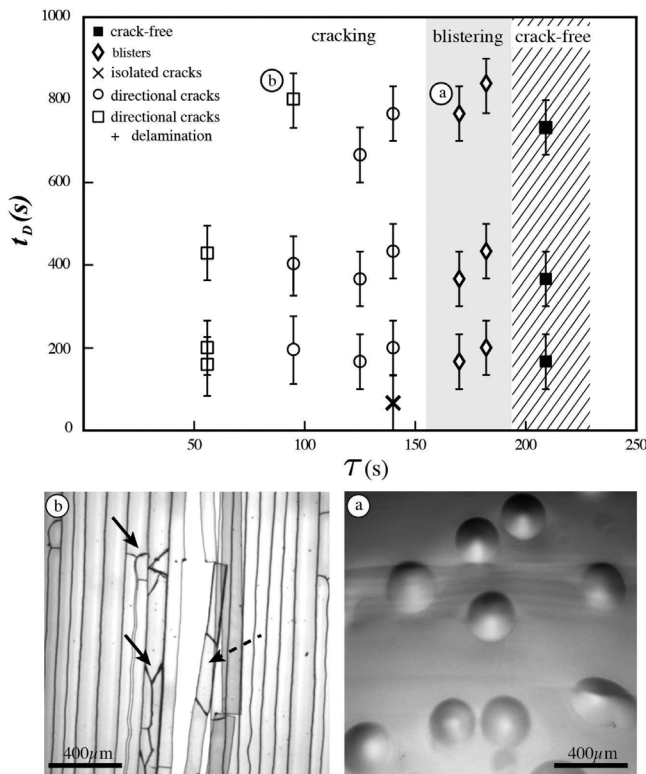


**FIG. 7.** Behavior of the coatings depicted in Fig. 6 when subjected to a wetting and drying process. Films of soft latex particles are still free of cracks (dashed area). Blistering occurs in the case of films of latex particles at  $T_g = 16, 25^\circ\text{C}$  (image a—observation in reflective light) in contact with water (grey area). Secondary crack formation (indicated by the plain arrows in image b) and possibly delamination process (indicated by the dashed arrow in image b) occur in the case of coatings of latex particles with  $T_g = 40$ . Such crack patterns are also observed in films of latex particles with  $T_g = 100^\circ\text{C}$  and silica particles (klebosol) particles in contact with water.

thickness,  $h$ . This simple model predicts a linear dependence of the crack spacing upon the coating thickness, which is in agreement with the results shown in Fig. 6(f). Data are shown for coatings exhibiting a network of parallel cracks during the drying (particles with  $T_g$

$= 40, 100^\circ\text{C}$ , silica klebosol and HS). The values of the elastic modulus are reported in Tables II and III,  $a$  is of the order of the particle size while the strain,  $\varepsilon \sim 0.1$ , is chosen as a fitting parameter.

In addition, in the case of nanosilica particles (HS), the pattern of cracks is followed by another mode of stress release, e.g., the delamination process, governed by the propagation of an interfacial crack at the film/substrate interface (image  $e$  in Fig. 6).

The diagram in Fig. 6, thus, report the aspect of coatings at the final stage of the drying. In the following, these coatings are subjected to the effect of a wetting and drying process.

**B. Films evolution after a wetting and drying process**

This section is devoted to the impact of the wetting and drying process of the coatings described in Sec. II E. Following the deposition of a water drop on the surface of a coating, different situations are encountered depending on the properties of the dry coatings.

In the case of a dry coating of soft latex particles with  $T_g = 0^\circ\text{C}$ , the surface of the coating is not permeable to the water as described in Sec. III A. As a result, the water droplet evaporates in the surrounding medium leaving a homogeneous coating surface (dashed region in the diagram in Fig. 7).

However, for the other systems (particles with  $T_g = 16, 25, 40, 100^\circ\text{C}$ , klebosol, and nanosilica HS), a part of the water imbibes the coatings. Hence, the wetting and drying process can lead to significant changes in the surface of the coating as reported in the diagram in Fig. 7. These patterns are detailed in the following.

**1. Blisters**

Starting from a homogeneous dry coating of latex particles with  $T_g = 16$  or  $25^\circ\text{C}$  [Fig. 8(a)], a water drop deposited on the surface spreads and partially soaks into the porous coating. The liquid invades the pores when the local pressure across the interface is smaller than the capillary pressure.<sup>24,25</sup> Observations show that circular blisters nucleate and grow at a delay time after the deposition of the water drop [Figs. 8(b) and 9(b)]. Blisters are not uniformly arranged spatially on the surface of the coating [images in Figs. 7(a) and 8(c)]. As a consequence, the density of defects possibly present at the substrate/latex film interface could act as blister nucleation sites.<sup>26,27</sup> Moreover, blisters exhibit similar growth dynamics. Indeed, for a coating made of

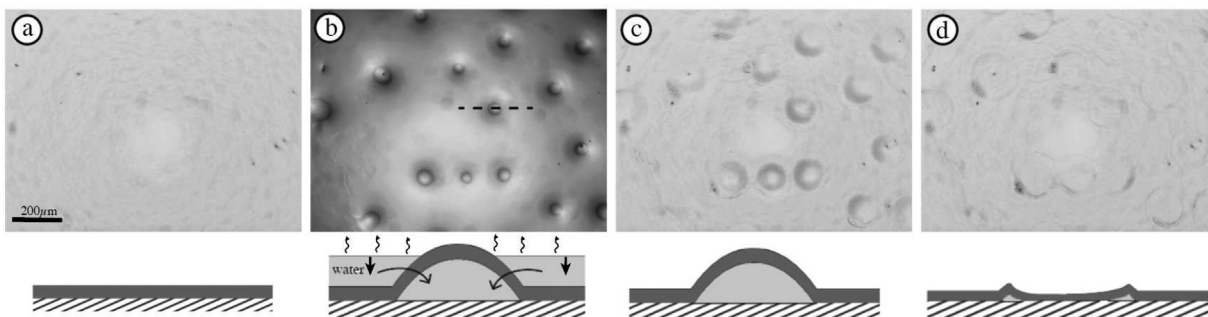


**FIG. 8.** Blistering—images in top view and sketches in side view. (a) Successive stages showing the growth and deflating of blisters during the wetting and drying process (coating of latex particles with  $T_g = 25^\circ\text{C}$ ,  $30\ \mu\text{m}$  thick). (a) Initial homogeneous surface of the dry coating. (b) and (c) Growth of circular blisters; the growth stops during the contact of the coating with water (the emergence of the blister apex from the evaporating water can be observed and is sketched along the dashed line). (d) The deflation of the blisters induced by the drying process results in a bumpy surface.

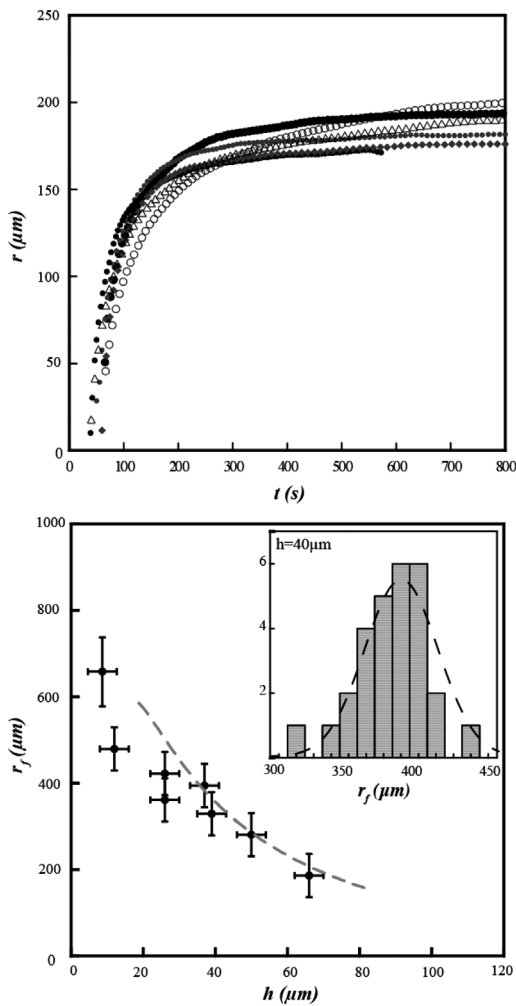


**FIG. 9.** Growth and final size of blisters induced by wetting and drying process of coatings of latex particles with  $T_g = 25^\circ\text{C}$ . (a) The blister radius,  $r$ , increases with time. (b) Blister radius,  $r_f$ , after the growth has stopped. [The dashed line corresponds to Eq. (7).] Inset: example of statistics on the  $r_f$  for a specific coating.

specific latex particles, the blisters start to grow nearly at the same time as shown in Fig. 9(a). (The time discrepancy between the blister’s nucleations is of the order of 10 s.) The blister radius increases with time resulting in the colloidal film delamination from the substrate [Fig. 9(a)]. The blisters initially grow fast; then, the growth slows with time. Moreover, the formation of blisters was monitored in fluorescence mode using fluorescent tracers (fluorescein) in the water in contact with the coating (Fig. 10). The enhanced fluorescence intensity inside the blisters qualitatively suggests that a part of the water and fluorescent tracers has concentrated in the internal volume of the blisters.

The osmotic flow in the film is a potential candidate to explain blistering. Hence, the presence of surfactant in the film (SDS) may provide an osmotic driving force for the diffusion of water through the film.<sup>28</sup> As the osmotic pressure increases, the coating starts to bulge. The deformation induced by the osmotic pressure competes with the

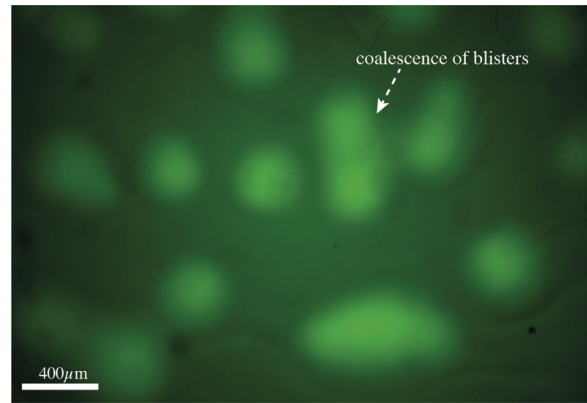


**FIG. 10.** Blistering using fluorescence mode. Observation of a coating of latex particles with  $T_g = 25^\circ\text{C}$  in contact with water that contains fluorescent tracers (fluorescein). The arrow indicates the coalescence of neighboring blisters as they grow.

adhesion of the film to the substrate and can result in instabilities. Indeed, once the osmotic pressure equalizes the fracture pressure,<sup>29</sup> the blister starts to grow.

Interestingly, the growth of the blister stops when the film surface is still in contact with the water. For a given coating of specific particles and thickness, the blisters exhibit comparable sizes at the final stage of the growth [see statistics in the inset of Fig. 9(b)]. Together with the imbibition and the evaporation the surface of the residual water recedes [Fig. 8(b)]. At the final stage of the drying process, the deflation of the blisters takes place. The coating exhibits a bumpy surface when depression takes place in the middle of the blisters and is surrounded by a circular rim [Fig. 8(d)].

The growth arrest of the blisters can be due to the decaying osmotic pressure.<sup>27</sup> In addition, we provide here the following mechanism based on the rheological properties of the coatings to explain the arrest of blister growth. Similarly to Eq. (3), the growth of a blister is governed by the release of the strain energy that has to overcome the adhesion of the film to the substrate. The resulting blister growth condition expresses as

$$1/2E\varepsilon^2h - \Gamma_{adh} \geq 0, \tag{4}$$

where  $E$  is the Young modulus of the film and  $\varepsilon$  is the strain of the film. The viscoelastic properties of the coating involve a decay of the elastic modulus, which can be approximated to a single-time relaxation process as<sup>30</sup>  $E(t) = E_0 \times \text{Exp}(-t/\tau)$ , where  $\tau$  is the relaxation time of the coating. The timescales involved in the blistering [Fig. 9(a)] and the viscoelastic properties of the coatings (Fig. 5 and Table II) suggest that after a delay-time, the strain energy is no more sufficient to overcome the adhesion of the film to the substrate. Hence, after delay  $t_{arrest}$  Eq. (4) is no longer valid. Given Eq. (4),  $t_{arrest}$  writes as

$$t_{arrest} = \tau \times \text{Ln} \left( \frac{E_0 \varepsilon^2 h}{2\Gamma_{adh}} \right). \tag{5}$$

Equation (5) highlights that the time at which the blisters stop to grow depends on the coating thickness,  $h$ . At the end of their growth, the size of the blisters is reported as a function of the coating thickness in Fig. 9(b).



The osmotic flow of water molecules through the surface of the blister of thickness,  $h$ , obeys the Darcy law.<sup>31</sup> Hence, a rough approximation based on the Darcy law gives the time variation of the blister radius as<sup>26</sup>

$$\frac{dr}{dt} \sim \frac{k}{\eta} \Phi \nabla P, \quad (6)$$

where  $k$  is the coating permeability assumed to be constant during the imbibition process,  $\eta$  is the water viscosity,  $\Phi$  is the density ratio between vapor and liquid water (at standard temperature and pressure), and  $\nabla P(t)$  is the pressure gradient in the film that is approximately related to the stress in the film as  $\nabla P \sim E\varepsilon/h$ . Hence, at the end of the growth process, that is at time  $t_{arrest}$ , Eqs. (5) and (6) give

$$r_f \sim \frac{k\Phi\tau(hE_0\varepsilon^2 - 2\Gamma_{adh})}{\eta h^2\varepsilon}, \quad (7)$$

where  $r_f = r(t_{arrest})$ . This simple model captures the decay of the final size of the blisters as a function of the coating thickness as shown by the experimental results in the range of thicknesses investigated in this work [Fig. 9(b)]. The strain,  $\varepsilon$ , is considered here as a fitting parameter which is estimated to be 0.09, as well as the Young modulus  $E_0 = 2\text{MPa}$ . Typically, a 10% change in  $\varepsilon$  leads to a 10% change in  $r_f$ . In addition, a 20% change in  $E_0$  leads to a 30% change in  $r_f$ . A lower value of the Young modulus is expected in the case of a coating saturated with water than in the case of an unsaturated one. This is highlighted by comparing the viscoelastic response of an unsaturated coating and saturated coating using nano-indentation testing in “sinusoidal mode” (see Appendix B).

For thin films, the growth of blisters is more rapid than in thicker ones in accordance with Eq. (6). The relaxation time of the coating,  $\tau$ , becomes greater than the diffusion time governing the blistering growth. Consequently, Eq. (7) is no more valid. Moreover, for thin coatings, it is more frequent that neighboring blisters coalesce (see example in Fig. 10).

## 2. Cracks

Different behaviors are expected during the wetting and drying process of coatings of stiffer particles.

First, the deposition of a water drop on the surface of thin coatings of latex with  $T_g = 40^\circ\text{C}$ ,  $5 \pm 2 \mu\text{m}$  thick, initially free of cracks, does not show any blistering contrarily to softer latex coatings. Indeed, the surface of the coating behind the receding contact line dries. Many microcracks form as shown in Fig. 11(b) indicating the formation of so-called drying cracks. At the final stage of the drying, a number of isolated cracks invade the coating surface [Fig. 11(c)]. These observations suggest that the medium can withstand the stresses developed during water imbibition during the wetting process. As an assumption, the strain due to the imbibition process is lower than the yield strain  $\sigma_y/E \sim 7 \times 10^{-2}$  (Table II). However, the capillary effect induced by the drying indicates that the coating is failing. This is supported in the case of thick coatings.

Indeed, the deposition of a water drop is now investigated on a thick coating of latex with  $T_g = 40^\circ\text{C}$ . Initially, the thick coating exhibits a network of parallel cracks as described in Fig. 12(a). The deposition process of a water drop does not itself result in the formation of new cracks. However, the drying process leads to the formation

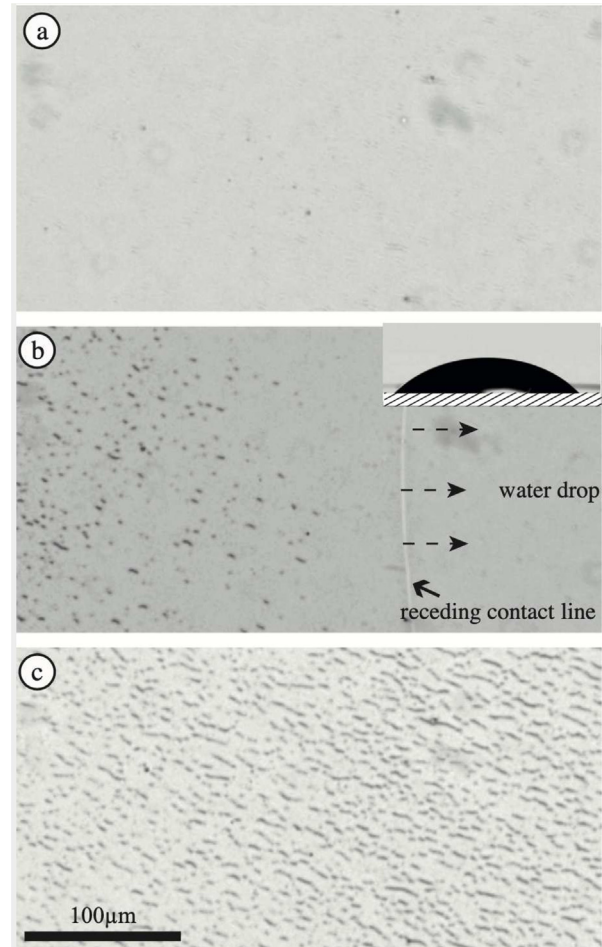


**FIG. 11.** Wetting and drying process of thin coatings of latex with  $T_g = 40^\circ\text{C}$ ,  $5 \pm 2 \mu\text{m}$  thick. (a) Initially, the coating is homogeneous. (b) Drying cracks are formed behind the receding contact line of the water droplet (inset: side view of a water drop on the coating surface). (c) A pattern of isolated cracks invades the surface of the coating at the final stage of the drying; the mean length of the cracks is  $7.9 \pm 0.3 \times \mu\text{m}$ .

of a secondary generation of cracks indicated by the arrows in Fig. 12(c). These cracks are perpendicular to the initial long one. They are few in number and more or less spaced. The dimensionless crack spacing,  $\lambda_2/h$ , is plotted as a function of the coating thickness in Fig. 13. The minimum spacing between these cracks obeys the Fracture Mechanics following Eq. (3):

$$1/2E\varepsilon^2\lambda a\lambda_2 = 2\Gamma h\lambda. \quad (8)$$

As a result, the value of  $\lambda_2/h$  for a given coating is reported by the dashed line in Fig. 13.

In addition to the expansion and contraction that occurs due to water absorption, the presence of water in the cracks can also cause them to grow. When water infiltrates a crack, it can exert a hydrostatic pressure that can cause the crack to open up further. This can lead to the formation of new cracks or the expansion of existing ones.

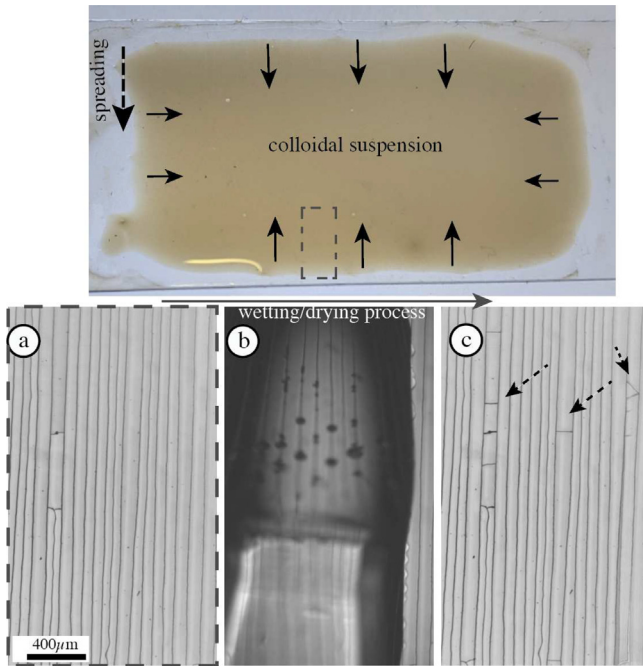


**FIG. 12.** Wetting and drying processes of thick coatings of latex with  $T_g = 40\text{ }^\circ\text{C}$ ,  $25 \pm 2\text{ }\mu\text{m}$  thick. (a) Initially, the coating shows a network of parallel cracks. (b) A water droplet is deposited on the surface of the cracked coating. (c) Only a few transverse cracks indicated by the dashed arrows are formed during the drying process.

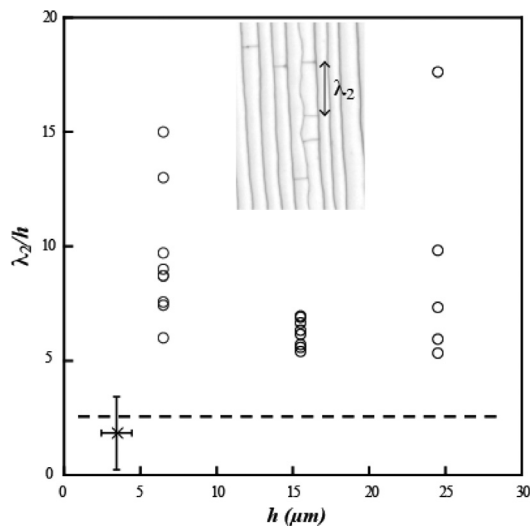


**FIG. 13.** Evolution of the crack pattern due to the wetting and drying process of coatings of latex with  $T_g = 40\text{ }^\circ\text{C}$ . The dimensionless spacing between the new cracks,  $\lambda_2/h$ , is plotted as a function of the coating thickness. The symbols  $\circ$  indicate the crack spacing between the second generation of cracks (inset image), while the symbols  $\times$  correspond to the mean spacing between the isolated cracks in Fig. 11(c). The dashed line corresponds to the crack spacing according to the fracture mechanics theory.

Finally, we consider the case of a brittle coating made of nanosilica particles (HS). During the drying, the film usually delaminates from the substrate as shown in the image *e* in Fig. 6. The influence of a wetting and drying process on the nanosilica coating is then considered by preventing the complete delamination of the film. In this way, a thin latex undercoat is preliminarily deposited on the glass slide to increase the adhesion between the silica film and the substrate. As a result, a partial delamination of the dry coating is shown in Fig. 14(a). The water deposition on the surface of such a cracked coating leads to the sudden formation of cracks as shown by the plain arrow in Fig. 14(a). As an assumption, the strain due to the imbibition process is higher than the yield strain  $\sigma_y/E \sim 2 \times 10^{-2}$  (Table II). This indicates that the strength of the coating is no longer sufficient to withstand the stress due to the imbibition process. Such a process is observed on coatings of different thicknesses. Furthermore, it seems that for sufficiently thick coatings, the cracks induced by imbibition are formed at the interface with the air and extend over a distance less than the total thickness of the layer close to the distance over which the imbibition has taken place [Fig. 14(b)].

### 3. Energy considerations

The occurrence of the instabilities reported in the present work depends on the way the coatings withstand the drying stresses. Hence, the coating behavior can be highlighted on the basis of the energies involved during the drying process. According to the fracture mechanics theory, the critical energy release rate,  $G_c$  of fracture is equal to the thermodynamically reversible work,  $\Gamma$ , used to create the new crack surfaces. Furthermore, the addition of viscoelastic dissipation modifies the energy balance such that

$$G_c = \Gamma + W, \tag{9}$$

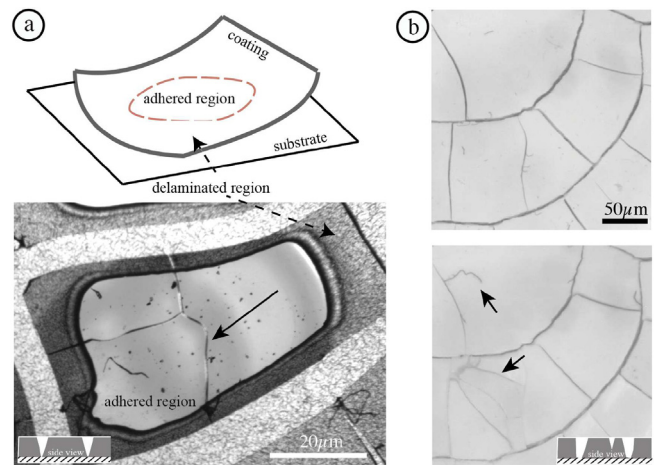


**FIG. 14.** Evolution of the crack pattern induced by water imbibition in a brittle coating of nanosilica (HS). (a) The coating thickness is  $15 \pm 3\text{ }\mu\text{m}$ : the plain arrow shows the new crack formed in the adhered region of the coating. (b) The coating thickness is  $28 \pm 3\text{ }\mu\text{m}$ : the new cracks do not extend through the whole thickness of the coating as sketched in side view.

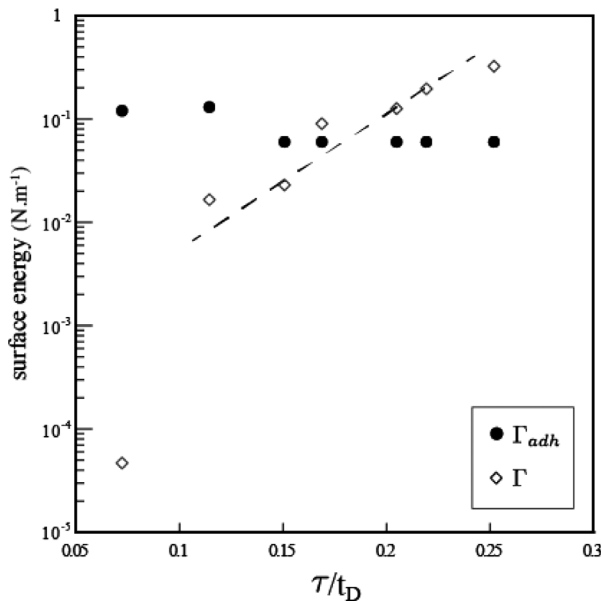


**FIG. 15.** Surface energy involved in different particulate coatings as a function of the dimensionless relaxation time,  $\tau/t_D$ . The surface energy indicated by the  $\diamond$  by the results from Eq. (11). The work of adhesion,  $\Gamma_{adh}$ , corresponds to the values reported in Table I. The dashed line is a guide for the eyes. Note that the lowest value of the surface energy corresponds to the coatings of silica particles whose size is ten times smaller than other particles.

where  $W$  is the energy dissipated in the film by internal deformations, such as particle deformation. This equation can be rewritten in the following form incorporating the elastic and viscous stresses:

$$\sigma_{el}\epsilon_c h = \Gamma + \sigma_{visc}\epsilon_c h. \tag{10}$$

The elastic stress scales as  $\sigma_{el} = E\epsilon_c$ , while the viscous stress scales as  $\eta d\epsilon/dt \sim \eta\epsilon/t_D$ , which includes the film viscosity,  $\eta = E\tau$ . Hence, the surface energy expresses as

$$\Gamma \sim Eh\epsilon_c(1 - \tau/t_D). \tag{11}$$

Using the values of the elastic modulus,  $E_2$ , and the relaxation time,  $\tau$ , from Tables II and III, the cracking condition is reported in Fig. 15 as a function of the coating relaxation time. When compared to the work of adhesion,  $\Gamma_{adh}$ , cracking appears to be energetically more favorable than blistering for coatings exhibiting a low relaxation time. Indeed, blistering results from a delamination process. This last occurs when the stored elastic strain energy overcomes the adhesion energy of the coating attached to the substrate.

Note that behind the values of the work of adhesion reported in Table I, an important part of the adhesion between the particulate coating and the substrate is due to the capillary process close to the coating/substrate interface. Indeed, air-in-liquid capillary bridge can exist in the porous structure, in the vicinity of the substrate. Such capillary bridges can be responsible for strong attractive interaction.<sup>32</sup>

#### IV. CONCLUSION

Drying films of latex or silica particles results in either crack-free or inhomogeneous coatings. In any case, the capillary effect

can generate instabilities such as cracks or blisters indicating that the coating is failing. One of the main properties determining the quality of paint from its deposition to its sustainability (failure) is the capacity of the particles to deform. Indeed, the excess strain energy arises from the competition between the drying-induced shrinkage of the deposit and its adhesion to the substrate. We show that the drying can yield continuous coatings with no porosity, uniform porous coatings, or the formation of cracks causing the final film to be non-uniform. The resulting coatings are then subjected to a wetting and drying process. The response of the coatings depends on their visco-elasto-plastic properties. In particular, in the case of porous films composed of soft particles, the wetting and drying processes lead to the formation of blisters. These last grow and reach a well-defined size, which is analyzed experimentally and by considering the energies involved.

#### ACKNOWLEDGMENTS

This work was benefited from a French State Grant “BOGUS” ANR-19-CE06-0030-02. I acknowledge J. Amarni, A. Aubertin, L. Auffray, C. Manquest, and R. Pidoux (FAST-University Paris-Saclay) for engineering and technical support.

#### AUTHOR DECLARATIONS

##### Conflict of Interest

The authors have no conflicts to disclose.

##### Author Contributions

**Ludovic Pauchard:** Conceptualization (lead); Formal analysis (lead); Validation (lead); Writing – original draft (lead); Writing – review & editing (lead).

#### DATA AVAILABILITY

The data that support the findings of this study are available from the corresponding author upon reasonable request.

#### APPENDIX A: ESTIMATION OF THE YIELD STRESS USING INDENTATION TESTING

The compressive yield stress of the dry layers is estimated using indentation tests. Initially, zero, the applied force on each sample is increased until reaching a maximum force  $F_{max}$  before unloading the sample (Fig. 16). In this way the following semi-empirical relationship is used as<sup>33</sup>  $\sigma_Y = \frac{F_{max}}{2.8A}$ , where  $A$  is the surface contact between the indenter and the material area of indentation and equals to

$$A = 24.5h_c^2 + 500.10^{-6}h_c,$$

where  $h_c$  is the contact depth depending upon the maximum force applied  $F_{max}$ :

$$h_c = h_{max} - \alpha F_{max}/S_{max}$$

and  $\alpha = 0.74$  is a geometric factor.

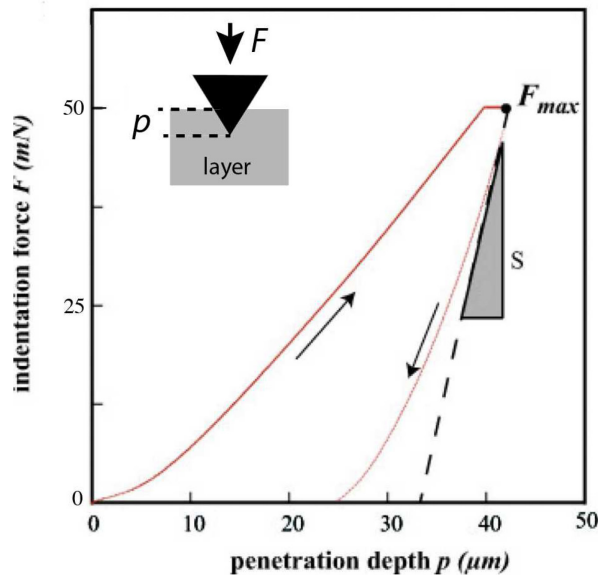


FIG. 16. Typical load-displacement curve resulting in the indentation force  $F$  as a function of the penetration depth  $p$ .  $S$  indicates the slope of the unloading curve at maximum applied force  $F_{max}$ .

APPENDIX B: VISCOELASTIC BEHAVIOR OF IMMERSed COLLOIDAL COATINGS USING DYNAMIC MECHANICAL ANALYSIS

Nano-indentation testing is used for the determination of the viscoelastic properties of a coating whose surface is in contact with water. Particularly, the “sinusoidal mode” is used for the determination of the storage,  $E'$ , and the loss,  $E''$ , moduli. The oscillation

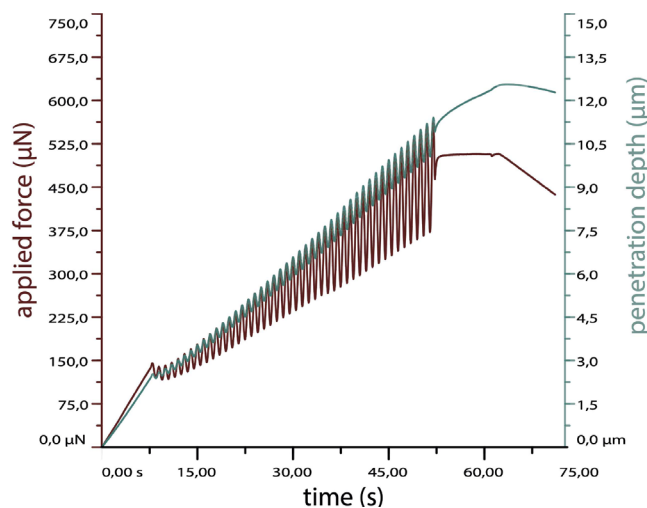


FIG. 17. Storage,  $E'$ , and loss,  $E''$ , moduli of coatings of latex  $T_g = 25\text{ }^\circ\text{C}$  whose surface is in contact with water. Typical load and indentation depth profile over time by using a low-magnitude oscillating force superimposed onto the quasi-static force signal. Maximum load:  $500\text{ }\mu\text{N}$ ; loading and unloading rate:  $500\text{ }\mu\text{N}/\text{min}$ ; sinus frequency  $1\text{ Hz}$ ; sinus amplitude:  $300\text{ }\mu\text{N}$ .

TABLE IV Storage,  $E'$ , loss,  $E''$ , and moduli using sinusoidal mode method.

$T_g$ ( $^\circ\text{C}$ )	$E'_{dry}$ (MPa)	$E'_{dry}'$ (MPa)	$E'_w$ (MPa)	$E'_w'$ (MPa)
0	$16.59 \pm 0.13$	$3.4 \pm 0.08$	...	...
16	$30.30 \pm 0.21$	$10.12 \pm 0.14$	$1.29 \pm 1$	$0.31 \pm 0.09$
25	$52.11 \pm 0.13$	$25.08 \pm 0.15$	$3.25 \pm 1.2$	$3.11 \pm 0.11$
40	$142.08 \pm 0.05$	$75.71 \pm 0.06$	$101 \pm 0.08$	$49 \pm 0.05$
100	$201.12 \pm 0.05$	$51.25 \pm 0.03$	$140 \pm 3$	$32 \pm 0.05$
Klebosol	$690 \pm 0.03$	$202 \pm 0.05$	$125 \pm 0.05$	$152 \pm 0.09$
HS	$1101 \pm 0.05$	$280 \pm 0.05$	$910 \pm 0.6$	$190 \pm 0.4$

mode is applied during the hold period at a constant force. The penetration depth is measured as a function of the loading force, which oscillates with a defined frequency (see typical measurements in Fig. 17). Storage,  $E'$ , loss,  $E''$ , and moduli are reported in Table IV for different films. The index “dry” refers to dry films obtained at the beginning of the second “falling rate period,” while index “w” to the same coatings whose surface is in contact with water. The measurements on a dry film start at the beginning of the second “falling rate period” ( $\sim 9 \times 10^3\text{ s}$ ). The duration of the measurements is 60 s. Then, a volume of water is deposited at the surface of the film. The measurements on the resulting wet films start a few minutes later. The duration of the measurements is 60 s.

REFERENCES

- Di Giuseppe, A. Davaille, E. Mittelstaedt, and M. François, “Rheological and mechanical properties of silica colloids: From Newtonian liquid to brittle behaviour,” *Rheol. Acta* **51**, 451–465 (2012).
- B. S. Garrett, W. C. Prentiss, and J. D. Scott, “Factors affecting the leveling of latex paints,” *Ind. Eng. Chem.* **51**, 117 (1959).
- M. Doi, “Gel dynamics,” *J. Phys. Soc. Jpn.* **78**, 052001 (2009).
- L. Pauchard, B. Abou, and K. Sekimoto, “Influence of mechanical properties of nanoparticles on macrocrack formation,” *Langmuir* **25**, 6672–6677 (2009).
- Y. Bertho, B. D. Texier, and L. Pauchard, “Egg-speriments: Stretch, crack, and spin,” *Phys. Fluids* **34**, 033101 (2022).
- L. Pauchard, “Patterns caused by buckle-driven delamination in desiccated colloidal gels,” *Europhys. Lett.* **74**, 188 (2006).
- A. F. Routh and W. B. Russel, “A process model for latex film formation: Limiting regimes for individual driving forces,” *Langmuir* **15**, 7762–7773 (1999).
- A. F. Routh and W. B. Russel, “Deformation mechanisms during latex film formation: Experimental evidence,” *Ind. Eng. Chem. Res.* **40**, 4302–4308 (2001).
- C. Allain and L. Limat, “Regular patterns of cracks formed by directional drying of a colloidal suspension,” *Phys. Rev. Lett.* **74**, 2981–2984 (1995).
- E. R. Dufresne, D. J. Stark, N. A. Greenblatt, J. X. Cheng, J. W. Hutchinson, L. Mahadevan, and D. A. Weitz, “Dynamics of fracture in drying suspensions,” *Langmuir* **22**, 7144–7147 (2006).
- L. Goehring, J. Li, and P.-C. Kiatkirakajorn, “Drying paint: From micro-scale dynamics to mechanical instabilities,” *Philos. Trans. R. Soc., A* **375**, 20160161 (2017).
- A. W. C. Lau, M. Portigliatti, E. Raphael, and L. Leger, “Spreading of latex particles on a substrate,” *Europhys. Lett.* **60**, 717 (2002).
- C. J. Brinker and G. W. Scherer, “Drying,” in *Sol-Gel Science*, edited by C. J. Brinker and G. W. Scherer (Academic Press, San Diego, 1990), Chap. 8, pp. 452–513.
- J. Li, B. Cabane, M. Sztucki, J. Gummel, and L. Goehring, “Drying dip-coated colloidal films,” *Langmuir* **28**, 200–208 (2012).
- M. Ahearne, Y. Yang, A. J. El Haj, K. Y. Then, and K.-K. Liu, “Characterizing the viscoelastic properties of thin hydrogel-based constructs for tissue engineering applications,” *J. R. Soc., Interface* **2**, 455–463 (2005).
- F. Boulogne, L. Pauchard, F. Giorgiutti-Dauphine, R. Botet, R. Schweins, M. Sztucki, J. Li, B. Cabane, and L. Goehring, “Structural anisotropy of directionally dried colloids,” *Europhys. Lett.* **105**, 38005 (2014).

Downloaded from http://pubs.aip.org/aip/pof/article-pdf/doi/10.1063/5.0153415/17937586/067107\_1\_5.0153415.pdf

- <sup>17</sup>M. S. Tirumkudulu and W. B. Russel, "Cracking in drying latex films," *Langmuir* **21**, 4938–4948 (2005).
- <sup>18</sup>K. B. Singh and M. S. Tirumkudulu, "Cracking in drying colloidal films," *Phys. Rev. Lett.* **98**, 218302 (2007).
- <sup>19</sup>V. Lazarus and L. Pauchard, "From craquelures to spiral crack patterns: Influence of layer thickness on the crack patterns induced by desiccation," *Soft Matter* **7**, 2552–2559 (2011).
- <sup>20</sup>R. C. Chiu, T. J. Garino, and M. J. Cima, "Drying of granular ceramic films: I, Effect of processing variables on cracking behavior," *J. Am. Ceram. Soc.* **76**, 2257–2264 (1993).
- <sup>21</sup>W. P. Lee and A. F. Routh, "Why do drying films crack?," *Langmuir* **20**, 9885–9888 (2004).
- <sup>22</sup>M. I. Smith and J. S. Sharp, "Effects of substrate constraint on crack pattern formation in thin films of colloidal polystyrene particles," *Langmuir* **27**, 8009–8017 (2011).
- <sup>23</sup>X. Ma, J. Lowensohn, and J. C. Burton, "Universal scaling of polygonal desiccation crack patterns," *Phys. Rev. E* **99**, 012802 (2019).
- <sup>24</sup>E. W. Washburn, "The dynamics of capillary flow," *Phys. Rev.* **17**, 273–283 (1921).
- <sup>25</sup>M. Léang, F. Ott, F. Giorgiutti-Dauphine, L. Pauchard, and L.-T. Lee, "Imbibition and structure of silica nanoporous media characterized by neutron imaging," *J. Colloid Interface Sci.* **565**, 474–482 (2020).
- <sup>26</sup>R. P. Berkelaar, P. Bampoulis, E. Dietrich, H. P. Jansen, X. Zhang, E. S. Kooij, D. Lohse, and H. J. W. Zandvliet, "Water-induced blister formation in a thin film polymer," *Langmuir* **31**, 1017–1025 (2015).
- <sup>27</sup>S. Effendy, T. Zhou, H. Eichman, M. Petr, and M. Z. Bazant, "Blistering failure of elastic coatings with applications to corrosion resistance," *Soft Matter* **17**, 9480–9498 (2021).
- <sup>28</sup>L. N. Butler, C. M. Fellows, and R. G. Gilbert, "Effect of surfactant systems on the water sensitivity of latex films," *J. Appl. Polym. Sci.* **92**, 1813–1823 (2004).
- <sup>29</sup>The following equation which is based on Griffith's law, gives the fracture pressure as:  $P_c = 2E\Gamma_{adh}/(\pi\rho)$  where  $E$  is the Young's modulus of coating, and  $\Gamma_{adh}$  is the surface energy cost to create the two interfaces as a result of the interfacial crack, and  $\rho$  a characteristic size of the defect leading to the blister nucleation.
- <sup>30</sup>J. S. Sharp and R. A. L. Jones, "Swelling-induced morphology in ultrathin supported films of poly( $d,l$ -lactide)," *Phys. Rev. E* **66**, 011801 (2002).
- <sup>31</sup>G. O. Brown, "Henry Darcy and the making of a law," *Water Resources Res.* **38**, 11-1–11-12 (2002).
- <sup>32</sup>C. H. Mastrangelo, "Adhesion-related failure mechanisms in micromechanical devices," *Tribol. Lett.* **3**, 223–238 (1997).
- <sup>33</sup>J. Malzbender, J. Toonder, A. Balkenende, and G. With, "Measuring mechanical properties of coatings: A methodology applied to nano-particle-filled sol-gel coatings on glass," *Mater. Sci. Eng. R* **36**, 47 (2002).